ACS NANO

www.acsnano.org

Open Access

This article is licensed under CC-BY-NC-ND 4.0

ARTICLE

Cobalt-Doped Ceria Sensitizer Effects on Metal Oxide Nanofibers: Heightened Surface Reactivity for High-Performing Chemiresistive Sensors

Jong Won Baek, Seunghee Han, Sang Eun Lee, Jaewan Ahn, Chungseong Park, Jong Seok Nam, Yoon Hwa Kim, Euichul Shin, Minhyun Kim, Ji-Soo Jang, Jihan Kim, Hee Jung Park,* and Il-Doo Kim*

Cite This: *ACS Nano* 2024, 18, 19568−19580

Read Online

ACCESS | Metrics & More | Article Recommendations | Supporting Information

ABSTRACT: **Chemiresistive gas sensors based on semiconducting metal oxides typically rely on noble metal catalysts to enhance their sensitivity and selectivity. However, noble metal catalysts have several drawbacks for practical utilization, including their high cost, their propensity for spontaneous agglomeration, and poisoning effects with certain types of gases. As such, in the interest of commercializing the chemiresistive gas sensor technology, we propose an alternative design for a noble-metal-free sensing material through the case study of Co-doped ceria ($Co-CeO_2$) catalysts embedded in a SnO_2 matrix. In this investigation, we utilized electrospinning and subsequent calcination to prepare $Co-CeO_2$ catalyst nanoparticles integrated with SnO_2 nanofibers (NFs) with uniform particle distribution and particle size regulation down to the sub-2 nm regime. The resulting $Co-CeO_2$@SnO_2 NFs exhibited superior gas sensing characteristics toward isoprene (C_5H_8) gas, a significant biomarker for monitoring the onset of various diseases through breath diagnostics. In particular, we identified that the $Co-CeO_2$ catalysts, owing to the transition metal doping, facilitated the spillover of chemisorbed oxygen species to the SnO_2 sensing body. This resulting in the sensor having a 27.4-fold higher response toward 5 ppm of C_5H_8 (compared to pristine SnO_2), exceptionally high selectivity, and a low detection limit of 100 ppb. The sensor also exhibited high stability for prolonged response−recovery cycles, attesting to the strong anchoring of $Co-CeO_2$ catalysts in the SnO_2 matrix. Based on our findings, the transition metal-doped metal oxide catalysts, such as $Co-CeO_2$, demonstrate strong potential to completely replace noble metal catalysts, thereby advancing the development of the commercially viable chemiresistive gas sensors free from noble metals, capable of detecting target gases at sub-ppm levels.**

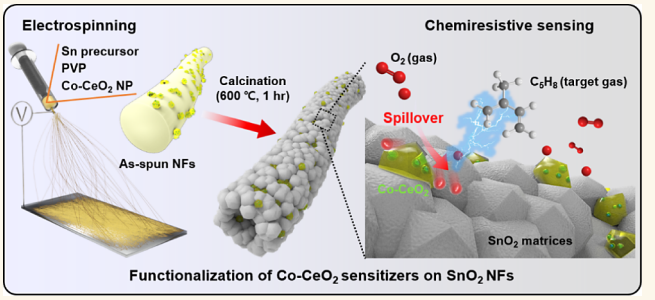

KEYWORDS: *cerium oxide, doping, metal oxide, electrospinning, gas sensor*

The high valuation of the gas sensor market at USD 2.90 billion in 2023, coupled with optimistic predictions to reach USD 5.49 billion by 2030, reflects the burgeoning demand for cutting-edge chemiresistive sensors based on metal oxides.[1] Importantly, to simultaneously achieve high sensitivity and selectivity standards to satisfy this demand,[2] the metal oxides serving as the sensing layer are often decorated with sensitizers to enhance surface reactivity between the metal oxide surface and target analyte. This enhancement stems from the operational principle of metal oxide-based sensors, which involves measuring the resistance change of the sensing layer as a result of the interaction between target gases and adsorbed oxygen species (O_2^-, O^-, O^{2-}) on the oxide surface.[3] In this regard, maximizing the number of adsorbed oxygen species at a given operating temperature is crucial for bolstering the surface reactivity of metal oxides toward the target gas. One reliable strategy is to functionalize noble metal nanoparticles (NPs) onto the oxide surface, as these catalytic NPs promote the oxidation of

Received: March 6, 2024
Revised: June 18, 2024
Accepted: June 20, 2024
Published: July 16, 2024

Downloaded via KOREA ADVANCED INST SCI AND TECHLGY on July 30, 2024 at 08:25:16 (UTC).
See https://pubs.acs.org/sharingguidelines for options on how to legitimately share published articles.

ACS Publications

© 2024 The Authors. Published by American Chemical Society

https://doi.org/10.1021/acsnano.4c03168
ACS Nano 2024, 18, 19568−19580

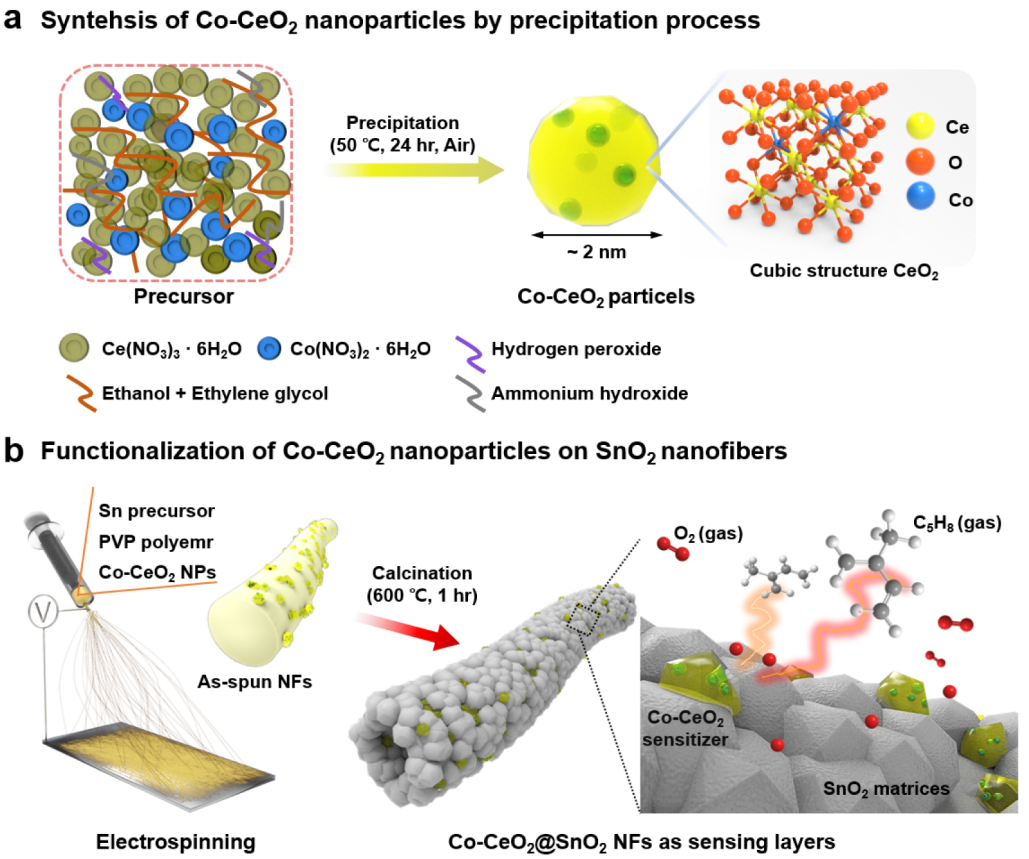

Figure 1. Schematic illustration of the overall synthesis process. (a) Synthesis of Co−CeO_2 NPs by precipitation process. (b) Functionalization of the Co−CeO_2 NPs on SnO_2 NFs through electrospinning.

atmospheric oxygen molecules through a spillover process.[4−6] However, noble metal NPs still face critical issues, such as deactivation of the catalytic activity due to the poisoning effect, a propensity for aggregation at elevated temperatures, and the scarcity of noble metals in the Earth's crust.[7−10] These challenges emphasize the necessity for alternative non-noble metal-based sensitizers to provide practical solutions, aiming to enhance sensing performance and achieve cost-effectiveness for commercialization.

To this end, lanthanides and their derivatives have gained considerable attention in various applications due to their distinct potential and advantages as alternatives to noble metals, which are more abundant in nature and exhibit superior resistance to gas poisoning.[11−13] In particular, ceria (CeO_2) is promising due to its vastly different redox properties, high oxygen conductivity, and thermochemical stability.[14,15] Based on these, CeO_2 has been reputed to be an ideal material for chemiresistive sensors, as both the main sensing layer and the sensitizer.[16,17] In addition, doping with transition metal atoms provides additional avenues to modify the surface chemistry of CeO_2 and improve their catalytic activity as heterogeneous catalysts.[18,19] As a sensitizer in chemiresistive sensor applications, transition metal-doped CeO_2 as a sensitizer offers three major advantages. First, dopants modify the electronic structure of CeO_2 to reduce the oxygen vacancy formation energy, facilitating the dissociation of chemisorbed oxygens and generating active oxygen species.[20] Second, transition metals and CeO_2 introduce additional active sites, enhancing oxidation activity and selectivity when interacting with target analytes. Third, strong metal−oxygen interactions between transition metal atoms and the oxygen atoms of the CeO_2 matrix contribute to increased stability and cyclability. Nevertheless, these CeO_2 catalysts have rarely been utilized as reaction promoters in chemiresistive sensors due to the lack of reliable functionalization strategies. It is imperative that these sensitizers be uniformly functionalized on the metal oxide-based sensing layer with a high degree of control if the objective is to elucidate the direct influence of transition metal doping on maximizing the reactivity of surface oxygens.

Functionalizing catalytic sensitizers on one-dimensional (1D) metal oxide nanofibers (NFs) by electrospinning is an emerging strategy to enhance the catalytic performance and obtain a nanostructure with a large surface area and high porosity.[21−23] Previous studies have demonstrated the functionalization of host oxide NFs with as-prepared perovskite oxides and ex-solution catalysts, leading to improved sensing properties.[24−26] However, achieving high dispersity and small sizes in electrospun sensing layers remained difficult, primarily due to the high temperatures necessary for the bulk synthesis of CeO_2 catalysts. These include methods such as coprecipitation, hydrothermal, and combustion,[27−31] which often lead to excessive grain growth and resultant particle sizes of 100 nm or larger. Aside from the issues with particle size, incorporating powder-form CeO_2 catalysts into the electrospinning solutions introduces the risk of poor redispersion, particle aggregation, and nozzle blockages, all of which lead to a poorly regulated final product.

In this work, we demonstrate the precipitation synthesized Co-doped CeO_2 NPs decorated onto SnO_2 NFs (Co−CeO_2@

https://doi.org/10.1021/acsnano.4c03168
ACS Nano 2024, 18, 19568−19580

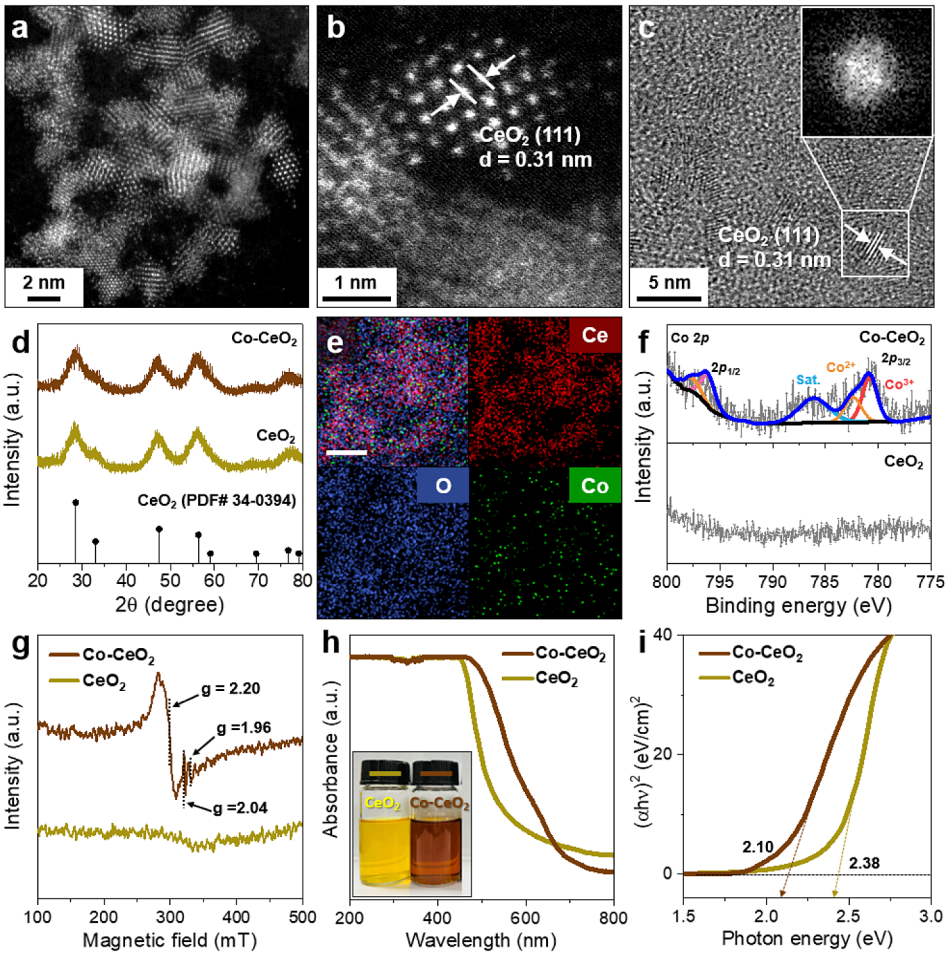

Figure 2. Characterization of Co−CeO_2 NPs. (a) Low magnification STEM image of Co−CeO_2 NPs. (b) High magnification STEM image of Co−CeO_2 NPs. (c) HRTEM image and inset showing the fast Fourier transform (FFT) patterns of Co−CeO_2 NPs. (d) XRD patterns showing the reflections of the CeO_2 structure. (e) EDS mapping images of Ce, O, and Co in the Co−CeO_2 NPs (scale bar 5 nm). (f) *Ex situ* XPS spectra of pristine CeO_2 and Co−CeO_2 NPs in the vicinity of Co 2*p*. (g) EPR spectrum of CeO_2 and Co−CeO_2 NPs. (h) UV−vis absorbance spectra and optical photograph of suspension of CeO_2 and Co−CeO_2 NPs (inset). (i) Tauc plots of CeO_2 and Co−CeO_2 NPs.

SnO_2 NFs), with the former serving as the sensitizer and the latter as the chemiresistive 1D sensing layer. A liquid-phase reaction with organic solvents (ethanol, ethylene glycol) as surface capping agents produced sub-2 nm Co−CeO_2 colloids as the capping agents effectively weakened interparticle interactions and suppressed grain growth. The colloidal solution could conveniently be added to the electrospinning solution by simply mixing Co−CeO_2, Sn precursors, and polymer, followed by electrospinning and calcination for the surface functionalization of Co−CeO_2 NPs on SnO_2 NFs. To evaluate the effectiveness of the Co−CeO_2 sensitizers in SnO_2 sensing layers, we comprehensively evaluated the sensing performance of the Co−CeO_2@SnO_2 NF-based sensor. The improved sensing performance for the target gas isoprene (C_5H_8) indicates that Co doping in the CeO_2 contributes to enhanced catalytic activity in comparison to undoped CeO_2. In addition, density functional theory (DFT) calculations, O_2 temperature-programmed desorption (O_2-TPD) analyses, and X-ray photoelectron spectroscopy (XPS) analyses were conducted to investigate the role of the Co−CeO_2 sensitizers in promoting the chemisorption behavior of oxygen species, their catalytic enhancement, and their effect on the enhanced sensing performance. These complementary techniques provided valuable insights and an understanding of the interactions between the Co−CeO_2 sensitizers and the target gases, contributing to the optimization and refinement of the sensor design. Moreover, our sensor exhibits sensing capabilities suitable for monitoring exhaled C_5H_8 gas, which serves as a biomarker in breath diagnostics, such as metabolic byproducts or blood cholesterol levels, with potential for real-world implementation. Altogether, our findings empower the development of robust chemiresistive gas sensors through effective sensitization by non-noble and cost-effective catalyst loading.

RESULTS AND DISCUSSION

Figure 1 illustrates the synthesis procedures for obtaining 2 nm Co-doped CeO_2 NPs (referred to as Co−CeO_2 NPs) as the catalysts for sensitizing the SnO_2-based chemiresistive sensors and their functionalization on the metal oxide NFs through electrospinning and subsequent calcination. Figure 1a describes how the Co−CeO_2 NPs could be obtained by the precipitation process (refer to Notes S1−S6). Here, ethanol and ethylene glycol were used for capping the surfaces of particles, effectively weakening the interparticle interactions and thus suppressing particle aggregation. In a typical synthesis, the Ce and Co precursors were dissolved in the mixed solvent, the pH of which was modulated using

https://doi.org/10.1021/acsnano.4c03168
ACS Nano 2024, 18, 19568−19580

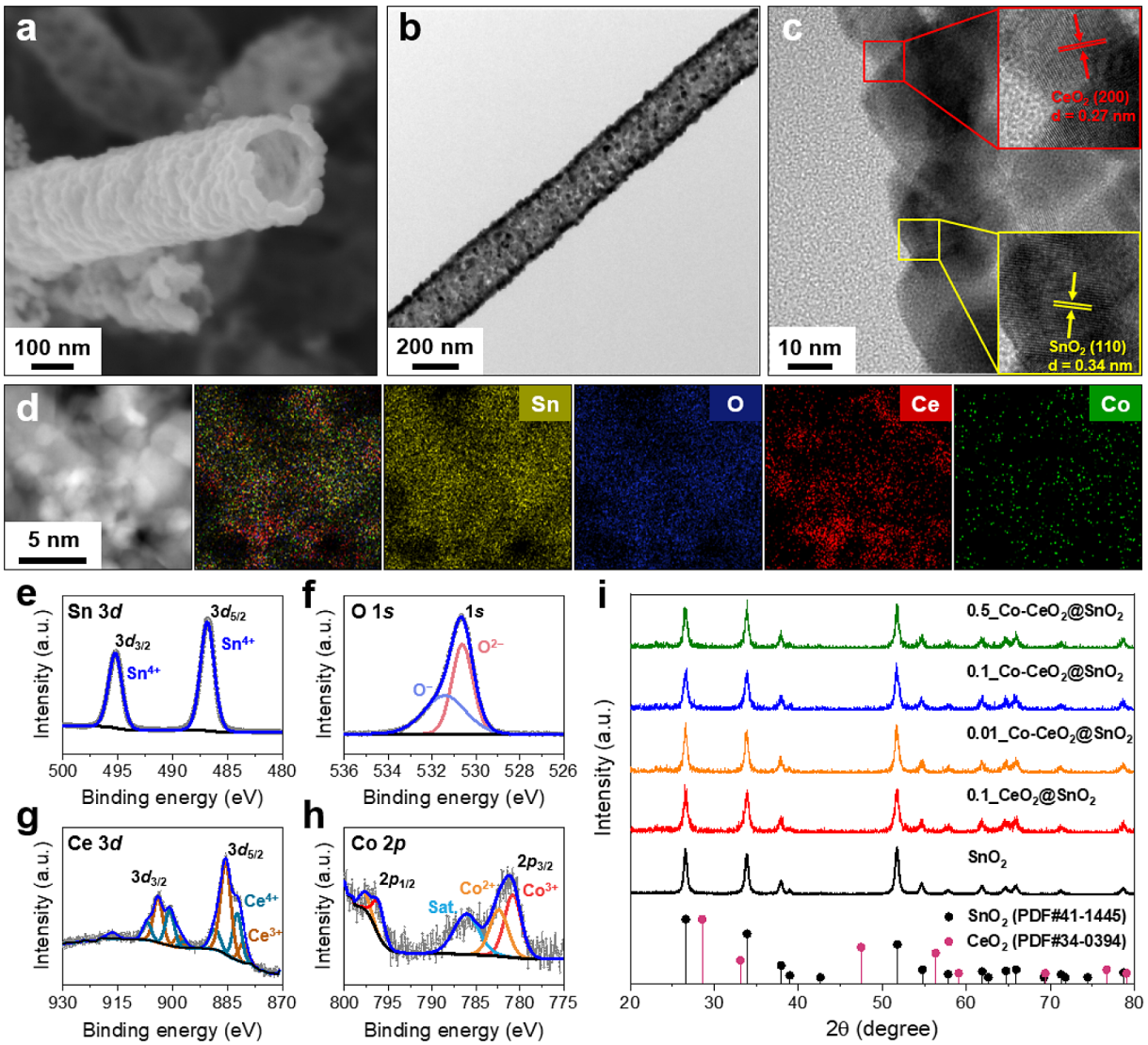

Figure 3. Characterization of the Co−CeO_2@SnO_2 NF. (a) SEM image of Co−CeO_2@SnO_2 NF after calcination. (b) TEM image of Co−CeO_2@SnO_2 NF. (c) HRTEM image of the Co−CeO_2@SnO_2 NF in (b) and magnified images (inset). (d) STEM image and EDS mapping images of overlay, Sn, O, Ce, and Co in the Co−CeO_2@SnO_2 NF (scale bar 5 nm). *Ex situ* XPS spectra of (e) Sn 3*d*, (f) O 1*s*, (g) Ce 3*d*, and (h) Co 2*p* in Co−CeO_2@SnO_2 NFs. (i) XRD patterns of pristine SnO_2 NFs and Co−CeO_2@SnO_2 NFs.

ammonium hydroxide, and a specific amount of hydrogen peroxide was added to trigger the reaction. After 24 h of reaction, the Co−CeO_2 NPs were obtained as a stable colloid. Then, the as-prepared colloidal solution was added to an electrospinning solution consisting of Sn precursors and the polymer matrix. The solution was electrospun into a polymer NF membrane containing Co−CeO_2 NPs and Sn species, which was calcined in an ambient atmosphere at 600 °C for 1 h to finally obtain the Co−CeO_2-decorated SnO_2 NFs (Figure 1b).

We first characterized the prepared colloidal Co−CeO_2 NPs to evaluate their applicability as a gas-sensitizing catalyst. Electron microscopy (EM) analyses were conducted on the as-obtained Co−CeO_2 NPs to assess their morphologies. For comparison, CeO_2 NPs have also been prepared using a similar protocol, just without Co, as the reference sample. The STEM images (Figures 2a,b and S1−S3) show that the average particle size of Co−CeO_2 NPs was determined to be 1.94 nm, with a standard deviation of 0.23, indicating that the organic solvents (ethanol and ethylene glycol) had regulated the formation of Co−CeO_2 colloids. The size distribution was similar to that of pristine CeO_2 NPs, implying that the morphology of NPs was not significantly affected by Co doping. In a high-resolution TEM image, Co−CeO_2 NPs show a diffraction pattern with a lattice spacing of 0.31 nm, which corresponds to the (111) plane of CeO_2 (Figures 2c and S4), confirming that the crystal structure of the matrix was maintained after doping.[32,33] Moreover, X-ray diffraction (XRD) patterns of the Co−CeO_2 NPs showed prominent peaks corresponding to the cubic structure of CeO_2 (JCPDF # 34-0394), not any different from that of pristine CeO_2, with a relatively high degree of crystallinity (Figure 2d). Notably, no peaks related to Co were observed, which suggests that there is almost no phase-separated Co, or at least the amount is below the detection limit of the XRD equipment. Scherrer analysis of peak broadening reveals that the average crystallite sizes of 1.98 nm for Co−CeO_2 NPs, which is similar to 2.04 nm for pristine CeO_2 NPs, estimated from the peaks corresponding to (111), (220), and (311) planes (Figure S5 and Table S1). Taken together, we could confirm that the Co atoms were

https://doi.org/10.1021/acsnano.4c03168
ACS Nano 2024, 18, 19568−19580

incorporated into the CeO_2 lattice without significant alterations to their crystallographic properties.

In conjunction with the EM-based physical morphology characterizations, the chemical properties of Co−CeO_2 NPs were studied using spectroscopic and diffraction analysis methods. Low-magnification energy-dispersive X-ray spectroscopy (EDS) mapping revealed the homogeneous distribution of cerium, oxygen, and cobalt throughout the entire particles without apparent separation (Figure 2e). XPS measurements were also conducted on the Co−CeO_2 NPs, revealing distinct peaks corresponding to Co 2*p* and indicating the concomitant presence of Co^{3+} and Co^{2+} valence states at 780.4 and 782.5 eV, respectively (Figure 2f).[34,35] With increasing Co doping levels from 0 (pristine CeO_2) to 7 at% Co, the intensity of the Co 2*p* peak showed a correlative increase (Figure S6a). In the Ce 3*d* region, the Ce 3*d* spectrum consisted of five spin−orbit split doublets (*u*: $3d_{3/2}$, *v*: $3d_{5/2}$) split by 18.6 eV. Ce cations in Co−CeO_2 NPs were in a mixed valence state of Ce^{3+} and Ce^{4+}, even though an ideally stoichiometric CeO_2 should consist solely of Ce^{4+} (Figure S6b). This is because the oxygen vacancies in CeO_2 NPs promote the formation of Ce^{3+} in order to maintain charge neutrality.[36] Moreover, it was observed that the intensity of the O 1*s* peak corresponding to adsorbed oxygen species on Co−CeO_2 NPs increased with higher Co doping levels (Figure S6c). This increase in adsorbed oxygen species provides enhanced catalytic activity in gas interaction reactions to improve the overall sensing performance. In addition, the presence of oxygen vacancies in CeO_2 promotes greater adsorption of oxygen species, facilitating the redox interaction between adsorbed oxygens produced on oxygen vacancies and reducing gas.[37] Therefore, it is evident that the Co dopants promote the formation of additional active oxygen species and provide the CeO_2-based sensitizer with favorable catalytic properties.

Since the Co dopants indubitably influenced the surface electronic structure of CeO_2, electron paramagnetic resonance (EPR) characterization was performed to obtain a detailed analysis of the chemical states of Ce species and oxygen vacancies CeO_2 and in Co−CeO_2 (Figure 2g). The reference EPR spectrum obtained from pristine CeO_2 NPs exhibited a low and broad signal, whereas intense and narrow resonance signals appeared at g = 2.20 in the case of Co−CeO_2 NPs, indicating the presence of Co ions.[38] Additionally, other resonance signals observed at g = 1.96 and g = 2.04 suggest increased amounts of Ce^{3+} and oxygen vacancies in Co−CeO_2, respectively.[36,39,40] These findings indicate that Co−CeO_2 exhibits multiple valences of Ce^{3+} and Ce^{4+} as well as abundant oxygen vacancies, resulting in enhanced activity for the oxidation of reducing gases. Furthermore, ultraviolet−visible (UV−vis) spectroscopy was performed to quantitatively evaluate the overall influence of the Co dopants on the electronic properties of CeO_2, with significant differences in absorbance spectra revealed between CeO_2 and Co−CeO_2 NP samples. Visually, the dispersed CeO_2 and Co−CeO_2 NP samples exhibited distinct pale yellow and orange colors, respectively (inset of Figure 2h), while maintaining a colloidal state without aggregation, with both samples exhibiting high transmittances (>95%) in the visible spectrum (Figure S7). The Tauc plots (inset) indicated an estimated decrease in the band gap energy from 2.38 eV for pristine CeO_2 to 2.10 eV for Co-doped CeO_2, owing to the energy levels provided by the Co dopant (Figure 2i). Specifically, the introduction of Co leads to an increased concentration of Ce^{3+} states, resulting in localized energy levels that are closer to the conduction band, reducing the band gap.[41,42] Altogether, the electronically modulated Co−CeO_2 NPs present a more favorable opportunity for facilitating surficial interactions with gas molecules.

The main advantage of this synthetic route, in comparison to high-temperature protocols, is that a high-quality colloidal solution of evenly doped catalyst NPs can be prepared at a relatively high concentration of approximately 1.4×10^{15} particles/mL. Importantly, these Co−CeO_2 NPs do not aggregate in the electrospinning solution owing to the organic-capped NP surfaces. This allows the highly concentrated Co−CeO_2 NPs to be uniformly dispersed, facilitating their incorporation into the electrospinning solution. As a result, a relatively high concentration of NPs can be used for the synthesis of chemiresistive sensing materials with high catalyst loading to facilitate a more efficient sensing behavior. As a result, through facile electrospinning and calcination processes, Co−CeO_2 NPs could be uniformly functionalized onto SnO_2 NFs. The scanning electron microscope (SEM) images in Figures 3a, S8, and S9 show the resultant Co−CeO_2 NPs-decorated SnO_2 NFs (Co−CeO_2@SnO_2 NFs) with a 1D fiber structure. Simultaneously, this procedure introduced porous sites and voids between the polycrystalline SnO_2 nanograin structures that facilitate gas diffusion, which was also confirmed by the TEM images in Figures 3b and S10. This morphological characteristic can be attributed to the hindrance of grain growth inhibition caused by well-dispersed Co−CeO_2 NPs, which effectively prevents the Ostwald ripening of SnO_2 during the calcination and results in a less dense structure.[24] Consequently, the Co−CeO_2@SnO_2 NFs showed a slight increase in the Brunauer−Emmett−Teller (BET) surface area and pore volume (20.2−28.9 $m^2\ g^{-1}$ and 0.053−0.113 $m^3\ g^{-1}$) in comparison to pristine SnO_2 NFs (14.4 $m^2\ g^{-1}$ and 0.038 $m^3\ g^{-1}$), as presented in Figure S11 and Table S2. The external regions of the 1D nanostructure were denser than the core regions, prompting the concentration of Co−CeO_2 NPs closer to the fiber surface. Ultimately, these aspects collectively make the Co−CeO_2@SnO_2 NFs one of the most rationally designed nanostructures for facilitating gas sensing applications.

Notably, the integrity of the Co−CeO_2 NP catalysts was not compromised during the fabrication process despite the involvement of a heat treatment step. For instance, the high-resolution TEM (HRTEM) image of the Co−CeO_2@SnO_2 NFs revealed two populations of grains having an interplanar spacing of either 0.34 or 0.27 nm, corresponding to the SnO_2 (110) and Co−CeO_2 (200) lattice planes, respectively (Figure 3c).[43] STEM imaging analyses accompanied by EDS mapping were also performed, as shown in Figures 3d and S12. The STEM image of Co−CeO_2@SnO_2 NFs clearly shows distinct contrast variations within the SnO_2 layers, indicating the homogeneous loading of the Co−CeO_2 phases on the surface of SnO_2 NFs by electrospinning and subsequent calcination process. The contrast differences among the grains indicate the presence of dissimilar elements with higher atomic numbers, such as cerium (Z_{Ce} = 58), leading to brighter appearances compared to lower atomic numbers, such as tin (Z_{Sn} = 50), from which we could discern the presence and distribution of Co−CeO_2 phases on the SnO_2 NFs. The mapping results further show the uniform distributions of Sn and O elements, corresponding to the SnO_2 NFs. The presence of Ce and Co elements corresponding to Co−CeO_2 NPs appears to be localized on the SnO_2 surface. In addition, XPS spectra of the

https://doi.org/10.1021/acsnano.4c03168
ACS Nano 2024, 18, 19568−19580

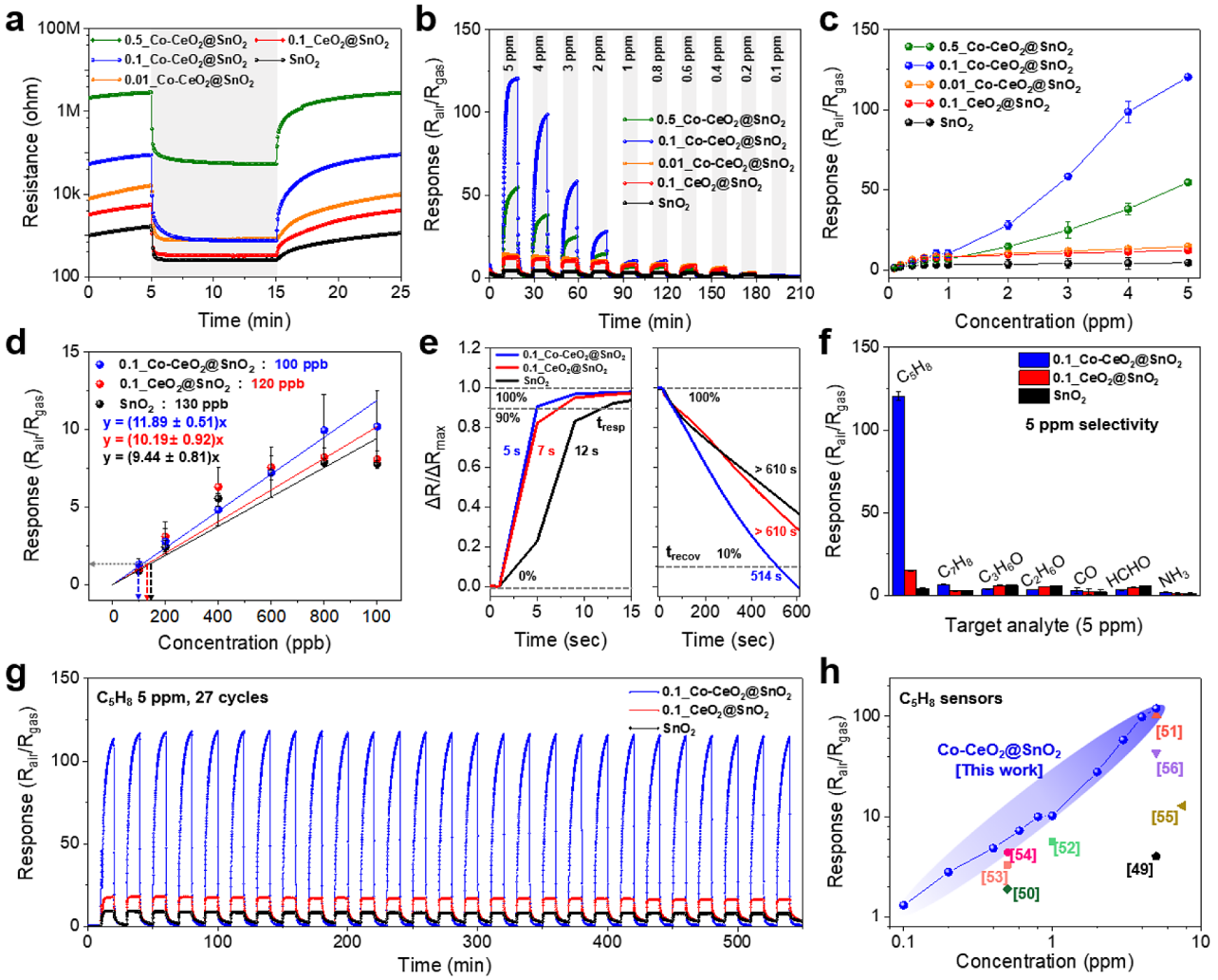

Figure 4. Chemiresistive sensing performance of Co−CeO_2 NPs functionalized SnO_2 NFs. (a) Electrical resistance profiles of the pristine SnO_2 NFs, 0.1_CeO_2@SnO_2 NFs, and 0.01, 0.1, 0.5_Co−CeO_2@SnO_2 NFs sensors at 5 ppm of C_5H_8 gas. (b) Dynamic C_5H_8 gas response in a concentration ranging from 0.1 to 5 ppm at 350 °C and (c) their corresponding plot of response *versus* gas concentration. (d) Linear regression results of responses extracted from the response values of SnO_2, 0.1_CeO_2@SnO_2, and 0.1_Co−CeO_2@SnO_2 NFs toward sub-ppm level (0.1, 0.2, 0.4, 0.6, and 0.8, 1 ppm) C_5H_8 gases. (e) Response and recovery times of SnO_2, 0.1_CeO_2@SnO_2, and 0.1_Co−CeO_2@SnO_2 NFs toward 5 ppm of C_5H_8 gas. (f) Selectivity chart of SnO_2, 0.1_CeO_2@SnO_2, and 0.1_Co−CeO_2@SnO_2 NFs toward 7 different analytes at 5 ppm. (g) Long-term reliability tests of SnO_2, 0.1_CeO_2@SnO_2, and 0.1_Co−CeO_2@SnO_2 NFs toward 27 cycles of exposure to 5 ppm of C_5H_8 under dry air. (h) Comparison of response values of the state-of-the-art C_5H_8 sensors compared with that of the Co−CeO_2@SnO_2 NF-based sensor.

Co−CeO_2@SnO_2 NFs showed characteristics of doublet peaks of Sn^{4+} at 486.8 and 495.2 eV, assigned to Sn $3d_{5/2}$ and Sn $3d_{3/2}$ peaks, respectively (Figure 3e),[44] while the deconvoluted O 1*s* spectra revealed two main peaks at 530.6 and 531.4 eV, each attributed to the lattice O atoms (O_{latt}) in SnO_2 and adsorbed oxygen (O^-) species, respectively (Figure 3f).[45] The XPS spectra of Ce 3*d* and Co 2*p* in Co−CeO_2@SnO_2 NFs are shown in Figure 3g,h, with no noticeable anomalies in comparison to the previously discussed XPS data for Co−CeO_2 NPs.

Moreover, we systematically investigated the crystallographic properties of the different SnO_2 NFs with varying concentrations of Co−CeO_2 additives. The relative weight percentages (wt %) of reference CeO_2 and Co−CeO_2 NPs in the prepared samples relative to the SnO_2 support layers were as follows: 0.1_CeO_2@SnO_2 (0.1 wt % of CeO_2 with respect to SnO_2 matrix), 0.01_Co−CeO_2@SnO_2, 0.1_Co−CeO_2@SnO_2, and 0.5_Co−CeO_2@SnO_2 (0.01, 0.1, and 0.5 wt % of Co−CeO_2 concentration relative to SnO_2 NFs). Note that, at these low levels of loading, the XRD diffraction pattern of the Co−CeO_2 NPs could not be discerned from the SnO_2 data (Figures 3i and S13). Therefore, we focused on the average crystallite sizes of SnO_2 grains in the pristine SnO_2 NF, 0.1_CeO_2@SnO_2 NF, 0.01_Co−CeO_2@SnO_2 NF, 0.1_Co−CeO_2@SnO_2 NF, and 0.5_Co−CeO_2@SnO_2 NF samples, calculated by the Scherrer equation using (110), (101), (200), and (211) planes. As a result, the grain sizes were shown to remain in similar ranges of 12.7−15.7 nm, indicating that the structural properties were not significantly altered by the incorporation of Co−CeO_2 NPs (Figure S14). Taken together, it is evident that the proposed electrospinning-based strategy for loading precipitation-prepared Co−CeO_2 NPs on SnO_2 NFs is effective for preparing oxide sensing materials decorated with catalytic NPs in a general sense.

The sensitizing role of the Co−CeO_2 catalyst NPs in the SnO_2 sensing layers was experimentally demonstrated by

https://doi.org/10.1021/acsnano.4c03168
ACS Nano 2024, 18, 19568−19580

performing a series of chemiresistive sensing measurements in the presence of the target gas C_5H_8, essential for health monitoring and physiological assessment. For this experiment, the sensing materials, *e.g.*, Co−CeO_2@SnO_2 NFs, were first drop-coated on prefabricated alumina sensor substrates with interdigitated gold electrodes. Afterward, their sensing characteristics were analyzed using our homemade sensor setup with regulated gas injection through mass flow controllers (Figure S15). We hypothesized that the introduction of redox-active Co-doped CeO_2 in the oxide-based sensing layer would greatly boost the sensing performance to levels that are not anticipated in unadulterated CeO_2 or CeO_2 decorated with a single-phase catalyst. To explore this, we evaluated the sensing capabilities of pristine SnO_2, CeO_2@SnO_2, and Co−CeO_2@SnO_2 NFs. For Co−CeO_2@SnO_2 NFs, comparative experiments were conducted with various loading amounts of Co−CeO_2 NPs for optimization.

After analyzing the temperature-dependent sensing properties toward the target analyte in the temperature range from 200 to 450 °C (Figure S16), we determined the optimal temperature for sensing to be 350 °C based on the response values. At this temperature, we performed dynamic gas sensing experiments using five different sensors (*i.e.*, pristine SnO_2 NFs, 0.1_CeO_2@SnO_2 NFs, 0.01_CeO_2@SnO_2 NFs, 0.1_CeO_2@SnO_2 NFs, and 0.5_Co−CeO_2@SnO_2 NFs) monitoring the resistance changes in the respective sensors upon exposure to 5 ppm of C_5H_8 (Figure 4a). Initially, the 0.1_CeO_2@SnO_2 NFs showed a baseline resistance of 5.5 kΩ, which is 3.2-fold higher than that of pristine SnO_2 NFs (1.7 kΩ) due to the greater number of chemisorbed oxygen species on the surfaces of SnO_2 NFs contributed by the CeO_2 NPs. Furthermore, the baseline resistances of the 0.01, 0.1, and 0.5_Co−CeO_2@SnO_2 NFs gradually increased from 16.1 to 90.1 kΩ, then to 2.9 MΩ, indicating a higher density of chemisorbed oxygen molecules on the Co−CeO_2@SnO_2 NFs as a result of spillover effects induced by catalytic Co−CeO_2 NPs. The spillover effect of the Co−CeO_2 NPs was formally examined by comparative ultraviolet photoelectron spectroscopy (UPS) measurements performed on pristine SnO_2 NFs, 0.1_CeO_2@SnO_2 NFs, and 0.1_Co−CeO_2@SnO_2 NFs. The work function of pristine SnO_2 NFs was measured as 5.48 eV (Figure S17a−d), which decreased to 5.33 and 5.11 eV with the incorporation of CeO_2 and Co−CeO_2, respectively (Figure S17e−l). This decrease suggests the transfer of electrons from the Co−CeO_2 NPs to the SnO_2 sensing layers, supporting the formation of a heterojunction between SnO_2 and Co−CeO_2. Furthermore, as indicated by the prior EPR and UV−vis absorbance results (Figure 2f,g), it can be inferred that Co−CeO_2 NPs exhibit multivalence, such as Ce^{3+} states, and an increased formation of oxygen vacancies. This results in a decrease in the bandgap while forming localized defect energy levels that are in closer proximity to the conduction band.[41,42] This can result in activated electron layers that facilitate the adsorption of oxygen species, ultimately improving the sensing performance of Co−CeO_2@SnO_2 NFs and further reinforcing their effectiveness as a gas sensor. Moreover, the additional generation of oxygen adsorption sites by Co−CeO_2 NPs promotes the uptake of oxygen species, facilitating the occurrence of the oxygen spillover phenomenon. Consequently, this raises the concentration of chemisorbed oxygen on the surface of SnO_2 decorated with Co−CeO_2 NPs.

Upon exposure to 5 ppm of C_5H_8, the 0.1_Co−CeO_2@SnO_2 NFs showed an excellent response (R_{air}/R_{gas}) of 120.38, which was 27.4-fold higher than that of pristine SnO_2 NFs (R_{air}/R_{gas} = 4.39). In contrast, the response of 0.1_CeO_2@SnO_2 NFs was enhanced only 3.4-fold (R_{air}/R_{gas} = 15.12) compared to pristine SnO_2 NFs. This difference is attributed to the heterojunctions between the Co−CeO_2 and SnO_2, in which the Co dopant played an important role in amplifying the spillover effect. Furthermore, upon dynamic exposure of C_5H_8 in the range from 0.1 to 5 ppm (Figures 4b and S18), we found that the 0.1_Co−CeO_2@SnO_2 NFs exhibited superior C_5H_8 response over those based on 0.01_Co−CeO_2@SnO_2, 0.5_Co−CeO_2@SnO_2 NFs, across the entire concentration range, demonstrating that the optimal amount of the catalytic sensitizers results in a significant improvement of their sensing characteristics. With fewer Co−CeO_2 NPs as sensitizers, the surface reactivity of the SnO_2 sensing layer is not sufficiently improved. Conversely, excessive loading of the catalysts could block the active sites within the SnO_2 layer, resulting in a notable degradation of sensing properties. Furthermore, we prepared different sensors with varying amounts of Co doping in CeO_2 while maintaining the same weight percent of the Co−CeO_2 NPs in SnO_2 NFs to determine the appropriate Co doping levels for optimized gas sensing performance (Figure S19). After conducting comparative evaluations, we determined that the optimum condition was found to be 3 mol % Co-doped CeO_2 functionalized SnO_2 NFs (0.1_Co−CeO_2@SnO_2 NFs) for detecting 5 ppm of C_5H_8 at 350 °C.

Considering the potential development of the Co−CeO_2@SnO_2 NF-based sensors into a commercially viable product, we comprehensively evaluated their sensing performance using multiple different performance metrics, as follows. During the dynamic changes in electrical resistance, an apparent linear relationship was observed between the response and concentration range of 0.1−5 ppm for the sensors (Figure 4c). This relationship indicates that the Co−CeO_2@SnO_2 NFs could be utilized to reliably detect C_5H_8 gas, especially in the low concentration range from 0.1 to 1 ppm. The detection limit (LOD) was estimated based on the response value exceeding 1.2 for sub-ppm-level C_5H_8 gases (Figure 4d). The Co−CeO_2@SnO_2 NFs showed a detection limit value of 100 ppb C_5H_8, surpassing the LOD exhibited by pristine SnO_2 NFs (130 ppb) and CeO_2@SnO_2 NFs (120 ppb), owing to the effective modulation of electrical resistance through the accelerated spillover of chemisorbed oxygen induced by the Co dopant. The response and recovery times of the sensors were calculated for 5 ppm of C_5H_8 exposure (Figure 4e). The response times of the sensors were improved from 12 s for pristine SnO_2 NFs to 7 and 5 s for CeO_2- and Co−CeO_2-decorated SnO_2 NFs, respectively. Likewise, the recovery rates were also improved in 0.1_Co−CeO_2@SnO_2 (514 s) compared to 0.1_CeO_2@SnO_2 (>610 s) and pristine SnO_2 (>610 s). This can be attributed to the contribution of increased porosity in the NF structure, which provides more channels for gas diffusion as well as active surface sites.[46] Furthermore, the gas selectivity of the 0.1_Co−CeO_2@SnO_2 NFs was investigated against other types of gases (Figure 4f). In particular, the 0.1_Co−CeO_2@SnO_2 NFs showed excellent C_5H_8 selectivity against potential interfering gases such as toluene (C_7H_8), acetone (C_3H_6O), ethanol (C_2H_6O), carbon monoxide (CO), formaldehyde (HCHO), and ammonia (NH_3). On the contrary, pristine SnO_2 NFs could not dependably isolate the C_5H_8 response from those of the interfering gases. Moreover, 0.1_Co−CeO_2@SnO_2 NFs also showed excellent stability against 27 cyclic tests toward 5 ppm

https://doi.org/10.1021/acsnano.4c03168
ACS Nano 2024, 18, 19568−19580

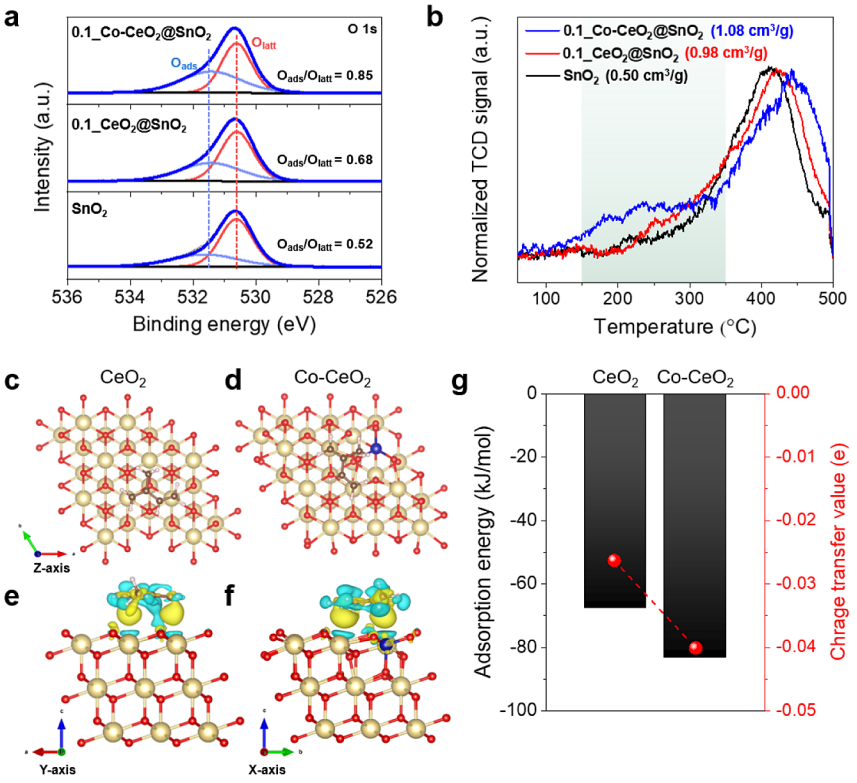

Figure 5. Investigation of catalytic role of Co−CeO_2 sensitizers. (a) *Ex situ* XPS spectra of pristine SnO_2, 0.1_CeO_2@SnO_2, and 0.1_Co−CeO_2@SnO_2 in the vicinity of O 1*s* peaks. (b) O_2-TPD profiles of pristine SnO_2, 0.1_CeO_2@SnO_2, and 0.1_Co−CeO_2@SnO_2. (c,d) The optimized binding configurations of CeO_2 (left) and Co−CeO_2 (right) toward the C_5H_8 molecule were calculated by DFT calculation (O: red, Ce: brown, Co: blue, C: dark brown, and H: white). (e,f) Side-view image of the charge density difference plot for CeO_2 (left) and Co−CeO_2 (right) interacting with C_5H_8 molecule (regions of charge accumulation in yellow and charge depletion in cyan). (g) Comparison of the calculated adsorption energy of C_5H_8 at CeO_2, Co−CeO_2, and their charge transfer values for the cases of C_5H_8.

of C_5H_8 (Figure 4g). Interestingly, even 5 weeks after the initial sample preparation, the 0.1_Co−CeO_2@SnO_2 NF-based sensor showed stable sensitivity performance during 193 cycles of exposure to 5 ppm of C_5H_8, as shown in Figure S20. In addition, as C_5H_8 is an important biomarker for breath diagnostics, the accurate detection of this species under highly humid conditions, such as exhaled breath, is crucial.[47,48] The effects of different humidity levels on our sensors can be observed in Figure S21. The dynamic resistance traces of our Co−CeO_2@SnO_2 sensors toward 5 ppm of C_5H_8 at 0, 25, 50, and 75% relative humidity show a slight decrease in response in humid air, attributed to the adsorption of water molecules that impede the reactions between C_5H_8 with the chemisorbed oxygen species of Co−CeO_2@SnO_2 NFs.[2,10,49] Nonetheless, this demonstrates that the C_5H_8 sensing performances of Co−CeO_2@SnO_2 NFs remain viable under various humid environments. Altogether, as shown in the summary table in Figure 4h and Table S3 comparing the sensing performances of Co−CeO_2@SnO_2 NFs to other reported C_5H_8 sensors,[50−57] the Co−CeO_2 NPs have effectively sensitized the SnO_2 sensing layers, enabling the selective detection of C_5H_8 gas with exceptional sensing performance. Most notably, this sensor efficiently responds to C_5H_8 using non-noble metals in lieu of noble metal catalysts, making significant progress in the realm of highly sensitive chemiresistive gas sensors. Despite comparing the gas detection performance of SnO_2 NFs with added noble metal Pt catalysts, the 0.1_Co−CeO_2@SnO_2 NF-based sensors still demonstrate superior C_5H_8 sensitivity (Figure S22).

Having established the effectiveness of the Co−CeO_2 catalysts, we further investigated the detailed sensitizing mechanisms through additional XPS analyses and O_2-TPD profiles, helping reveal the underlying chemistry of the chemisorption of oxygen species and selective gas adsorption facilitated by the Co−CeO_2 sensitizers. Indeed, the adsorption and activation of oxygen species on the Co−CeO_2@SnO_2 NFs were critical steps for facilitating efficient chemiresistive sensing. The properties of oxygen species were inevitably affected by oxygen vacancies and the presence of Co−CeO_2 NPs on the surfaces of SnO_2 sensing layers. The O 1*s* XPS spectra (Figures 5a and S23) revealed asymmetrical peaks corresponding to oxygen species chemically adsorbed by surface oxygen vacancies (O_{ads} at 531.4 eV) and lattice oxygen (O_{latt} at 530.6 eV).[45] The O_{ads}/O_{latt} ratio, calculated based on the respective integrated peak areas, showed significant increases in 0.1_Co−CeO_2@SnO_2 (0.85) and 0.1_CeO_2@SnO_2 (0.68) compared to pristine SnO_2 (0.52). This indicates that the 0.1_Co−CeO_2@SnO_2-based sensor, with a larger number of surface oxygen species, would exhibit the most sensitive response based on the aforementioned sensing performances. It is sufficient to demonstrate that a high density of oxygen species is chemisorbed on the surface of SnO_2 NFs, and based on the aforementioned O 1*s* XPS results of Co-doped CeO_2 from Figure S6c, the relative increase in the proportion of reactive oxygen species can be attributed to the enhanced spillover effects of decorated Co-doped CeO_2.[18,58] Meanwhile, comparing the desorbed oxygen profiles for each sample through O_2-TPD analyses revealed that the oxygen

https://doi.org/10.1021/acsnano.4c03168
ACS Nano 2024, 18, 19568−19580

species contribute significantly toward the gas response (Figure 5b). In the case of 0.1_Co−CeO_2@SnO_2, noticeable oxygen desorption was observed as a broad shoulder in the temperature range of 150−350 °C. On the other hand, the pristine SnO_2 only showed a peak related to the desorption of chemisorbed oxygen (~400 °C). It should be noted that below 150 °C, the dominant species are in their molecular form (O_2^-), while the atomic species (O^- and O^{2-}) are prevalent in the higher temperature region.[58−60] Consequently, these increased reactive oxygen atomic species formulated upon introducing the Co−CeO_2 NPs would serve as primary active sites for the adsorbed analytes to enhance the C_5H_8 response.

To support the experimental findings and rationalize the underlying mechanism behind the enhanced sensing properties in Co−CeO_2@SnO_2, we conducted DFT calculations to investigate the adsorption energies and conducted Bader charge analyses (Figures 5c−g and S24). First, adsorption energies of C_5H_8 on both CeO_2 and Co−CeO_2 surfaces were calculated for different possible configurations (Table S4). The results revealed that the adsorption energy of C_5H_8 on Co−CeO_2 (−83.5 kJ mol^{-1}) was higher compared to that of CeO_2 (−67.6 kJ mol^{-1}), indicating more favorable adsorption of the target analyte on the Co−CeO_2 surface (Figure 5g). Additionally, the charge density difference plot in Figure 5e,f, along with the Bader charge analysis in Figure 5g, indicates an increase in the absolute value of charge transfer from 0.0263 e for CeO_2 to 0.0401 e for Co−CeO_2. In chemiresistive sensors, adsorption and dissociation processes involve charge transfer between the target analyte and the catalytic layers, which affects the resistance of the sensing layers. Thus, a larger magnitude of charge transfer in Co-doped CeO_2 would indicate a significant reinforcement in the C_5H_8 adsorption and activation behavior compared to pristine CeO_2 NPs. Based on these findings, the improved sensing performance of Co−CeO_2@SnO_2 NFs toward C_5H_8 can be attributed to the improved catalytic properties of Co−CeO_2. Upon incorporation of Co−CeO_2 NPs SnO_2, the sensitizer starts to facilitate the dissociation of chemisorbed oxygen species on the sensing body and promotes favorable surficial interactions with C_5H_8. Therefore, it was anticipated that the Co−CeO_2@SnO_2 NF-based chemiresistive sensor would demonstrate a significant improvement in overall sensing performance compared to pristine SnO_2 NFs as well as any other pre-existing sensing materials. Additionally, Fe−CeO_2 and Ni−CeO_2 catalysts were functionalized onto SnO_2 as sensitizers and sensor measurements were conducted (Figure S25). We confirmed that using Fe−CeO_2 and Ni−CeO_2 as sensitizers also positively affects sensitivity enhancement compared to pristine SnO_2 NFs and CeO_2@SnO_2 NFs. However, the performance improvement was most pronounced when using Co−CeO_2 catalysts. Therefore, we chose to utilize the combination of Co−CeO_2, which offers the most superior sensing performance, albeit at a higher cost compared to other transition metals such as Fe and Ni. Nevertheless, the use of Co-doped CeO_2 remains still advantageous in terms of cost compared to noble metal elements (Pt, Pd, Ag, Au) (Table S5). Based on the aforementioned sensitizing mechanisms of the Co−CeO_2 NPs on SnO_2 NFs, it is important to emphasize that our transition metal-doped CeO_2 NPs offer an efficient approach for designing high-performance chemiresistive sensors without noble catalysts.

CONCLUSION

In the development of metal oxide-based chemiresistive gas sensors, incorporating catalytic sensitizers has traditionally relied on noble metal catalysts to enhance reactivity between the target gas and the sensing layer. While noble metals offer high catalytic activity, oxidation resistance, and corrosion resistance, their scarcity drives up sensor costs, and their susceptibility to agglomeration and poisoning effects can degrade sensing performance. To address these challenges, we propose an alternative sensitizer design using transition metal Co-doped ceria (Co−CeO_2) catalysts. Doping CeO_2 with Co enhances the spillover effect and increases oxygen adsorption, thereby accelerating the diffusion of oxygen species into the sensing layer. These catalysts were effectively integrated onto nanostructured SnO_2 NFs using electrospinning (Co−CeO_2@SnO_2 NFs). The Co−CeO_2@SnO_2 NF-based sensor demonstrates low detection limits (100 ppb), rapid sensing speed (5 s), and long-term stability over repeated sensing cycles for up to 550 min, indicating comprehensive improvement across all sensor performance metrics. Thus, this study presents a robust and rational design for chemiresistive sensors that effectively detect C_5H_8 through cost-effective sensitization, offering viable alternatives to noble metal catalysts. This achievement is expected to establish a foundational paradigm for future sensitizer designs, significantly advancing the field of high-performing gas sensors.

EXPERIMENTAL SECTION

Materials. Tin chloride dihydrate ($SnCl_2 \cdot 2H_2O$, 98%), *N*,*N*-dimethylformamide (DMF, 99.8%), acetic acid (99.7%), and polyvinylpyrrolidone (PVP, M_w = 1,300,000), and chloroplatinic acid hexahydrate ($H_2PtCl_6 \cdot 6H_2O$) were purchased from Sigma-Aldrich. Ethanol (99.5%), ethylene glycol (99.5%), ammonium hydroxide (30%), and hydrogen peroxide (34.5%) were obtained from Samchun. Cerium nitrate hexahydrate ($Ce(NO_3)_3 \cdot 6H_2O$, 99.95%) was purchased from GFS Chemicals. Cobalt nitrate hexahydrate ($Co(NO_3)_2 \cdot 6H_2O$, 99.9%) was received from Junsei. All chemicals were utilized as received without undergoing additional purification processes.

Preparation of CeO_2 NPs. 26.04 g of cerium nitrate hexahydrate was dissolved in a mixture of 60 mL of ethylene glycol and 240 mL of ethanol. The solution was stirred with a magnetic bar at 300 rpm for 30 min. Then, 1 mL of hydrogen peroxide was added to the mixed cerium precursor solution and stirred at 150 rpm for 20 min. Ammonium hydroxide was added to the solution to adjust the pH to 8.0−9.0. Then, the reaction temperature increased to 50 °C, and air was bubbled into the solution. The reaction was carried out for 24 h. As a result of this process, a yellow precipitate was formed. The solutions were washed with ethanol and centrifuged at 5000 rpm three times, each time for 10 min. Then, 8 mL of distilled water was added to the solution and mixed using a shaker for 5 min. After the mixing, a yellowish transparent solution was obtained.

Preparation of Co−CeO_2 NPs. Co−CeO_2 NPs were synthesized using the same method as the fabrication of CeO_2 NPs. Initially, cerium nitrate hexahydrate was dissolved in the mixture of solvents. In addition, the Co ion precursor was prepared in an amount that corresponds to the desired doping mol % concentrations relative to cerium (1, 3, 5, and 7%). Subsequently, a controlled amount of the Co ion precursor was injected into the reaction mixture using a micropipette. Afterward, the resulting solution was subjected to the same procedure described earlier for CeO_2 synthesis. Inductively coupled plasma optical emission spectroscopy (ICP-OES) was used to measure the Co content on Co−CeO_2 quantitatively.

Preparation of SnO_2 NFs, CeO_2@SnO_2 NFs, Co−CeO_2@SnO_2 NFs, and Pt@SnO_2 NFs. SnO_2 NFs were produced using electrospinning, with an initial solution formulated by dissolving 1.0

https://doi.org/10.1021/acsnano.4c03168
ACS Nano 2024, 18, 19568−19580

g of tin chloride dihydrate in 8 mL of DMF solvent. Next, 1.4 g of PVP polymer was added to the composite solution and stirred for 24 h. The resultant precursor solution was subsequently loaded into 20 mL plastic syringes and electrospun using a pump operating at a feeding rate of 5 μL min^{-1}, with a voltage of 16 kV, while maintaining a distance of 10 cm between the syringe nozzle tip and the drum collector. Following electrospinning, the as-spun composite fiber mats consisting of Sn precursor and PVP were calcined at 600 °C for 1 h, with a heating rate of 5 °C min^{-1}, in an ambient atmosphere to obtain crystalline SnO_2 NFs. For CeO_2-decorated SnO_2 NFs (CeO_2@SnO_2 NFs) and Co−CeO_2-decorated SnO_2 NFs (Co−CeO_2@SnO_2 NFs), different amounts of CeO_2 NPs and Co−CeO_2 NPs, respectively, were incorporated into the electrospinning solution containing the Sn precursor and PVP matrix polymer. For Pt catalyst-loaded SnO_2 NFs, a 0.2 M aqueous solution containing the Pt ion precursor was prepared, and a controlled amount of this solution was mixed with the electrospinning solution. The fabrication of CeO_2-decorated SnO_2 NFs and Co−CeO_2-decorated SnO_2 NFs, and Pt catalyst-loaded SnO_2 NFs followed the same experimental procedures for electrospinning and calcination steps without further modifications.

Fabrication of Gas Sensor and Evaluation of Sensing Performance. Gas sensors were fabricated on an alumina (Al_2O_3) substrate to measure the resistance variation of the prepared materials upon exposure to air and target analytes. Interdigitated Au electrodes with a width of 25 μm and a distance of 70 μm, along with a Pt heating wire on the other side, were printed on the alumina support, which had dimensions of 2.5 × 2.5 mm and a thickness of 0.2 μm. Next, 10 mg of the prepared materials were dispersed in 500 μL of ethanol, and the dispersed solutions were drop-coated onto the front side of the substrate. The resistance of the prepared gas sensors was evaluated using a custom-made gas sensor testing system. The system included a 16-channel multiplexer (34972A, Agilent), solenoid valves, and mass flow controllers (MFC). Before the gas was introduced, all the sensors were equilibrated under ambient conditions for 5 h. The exposure to gases followed a 10 min on/off interval. The humidity of the reference gas was controlled by redirecting a fraction of the gas stream into a water bubbler maintained at 37 °C. Subsequently, this humidified gas was mixed with the balance gas using the MFC. The operation temperature was controlled by adjusting the direct current (DC) voltage applied to the Pt heater using a DC power supply (E3654A, Agilent). The response and recovery times are characterized as the duration required for the resistance to attain 90% of the ultimate response ($(R - R_{min})/R_{max} \geq 0.9$) and the duration for the resistance to return to 10% of the final response ($(R - R_{min})/R_{max} \leq 0.1$), respectively. The collected data were processed by calculating the resistance ratio of R_{air}/R_{gas}, where R_{air} represents the baseline resistance in ambient air and R_{gas} corresponds to the resistance during gas injection. This ratio serves as the gas response of the sensors, indicating their sensitivity to the target gas.

Characterization. Ultraviolet−visible (UV−vis) spectra were obtained using a Lambda 1050 (PerkinElmer). The crystal structures of the SnO_2, CeO_2-decorated SnO_2, and Co−CeO_2-decorated SnO_2 were confirmed using a high-resolution powder X-ray diffractometer (XRD) (RIGAKU, SmartLab) equipped with Cu Kα radiation (λ = 1.5418 Å). The average crystallite size of CeO_2, Co−CeO_2, SnO_2, CeO_2-decorated SnO_2, and Co−CeO_2-decorated SnO_2 was calculated using the Scherrer equation, which is defined as follows: $d = 0.9\lambda/\beta\cos\theta$, where d is the average crystallite size, λ is the wavelength of the incident beam (0.154 nm), θ is the Bragg angle, and β is the line broadening factor at half of the maximum intensity (fwhm) in radians. The morphologies of the samples were characterized using a scanning electron microscope (SEM, SU5000, Hitachi), while the microstructures were investigated using a 300 keV field emission transmission electron microscope (TEM) (F30 supertwin, Tecnai). Scanning transmission electron microscopy (STEM) and energy dispersive spectroscopy (EDS) elemental mapping analysis were conducted with aberration-corrected TEM (JEMARM200F, JEOL). X-ray photoelectron spectroscopy (XPS) (Axis-Supra, Kratos) with Al K radiation was employed to investigate the chemical bonding states. Ultraviolet photoelectron spectroscopy (UPS) measurements were performed using an AXIS-Supra with a He I discharge lamp emitting photons with an energy of 21.2 eV. The doping amount of Co compared to Ce was measured using an Agilent ICP-OES 720 instrument. The Brunauer−Emmett−Teller (BET) surface area with pore size distribution was measured using N_2 adsorption/desorption isotherms used by a Tristar 3020 instrument from Micromeritics. O_2 temperature-programmed desorption (O_2-TPD) experiments were performed using AutoChem II to quantitatively evaluate the amount of desorbed oxygen. In each experiment, 100 mg of samples was positioned on a quartz bed and subjected to pretreatment with air at room temperature. The temperature was then gradually increased up to 500 °C at a ramping rate of 10 °C min^{-1}. Electron paramagnetic resonance (EPR) measurements were conducted at room temperature utilizing a JES-FA100 instrument, maintaining consistent conditions such as a microwave frequency of 9.21 GHz, microwave power of 1 mW, and modulation frequency of 100 kHz. The g-factor was derived by computation using the equation $h\nu = g\beta H$, wherein h denotes Planck's constant, H represents the applied magnetic field, and β stands for Bohr's magneton.

DFT Calculations. DFT calculations were performed using Vienna Ab initio Simulation Program (VASP) software version 5.4.1.[61,62] The Perdew−Burke−Ernzerhof (PBE) exchange−correlation functional and projector-augmented wave (PAW) pseudopotentials were utilized in the calculations.[63] To account for van der Waals interactions, the PBE-D3 method of Grimme was used, and dipole corrections were implemented to alleviate artificial potential gradients near periodic boundaries.[64] The bulk structure of CeO_2 was obtained from the Materials Project database.[65] The CeO_2 surface was cleaved to expose the (111) facet,[66] and a 9 atomic layers model with a 20 Å vacuum gap perpendicular to the surface was prepared, consisting of 27 Ce atoms and 54 O atoms. The Co−CeO_2 surface was obtained by substituting one Co atom in the CeO_2 surface, resulting in a structure comprising 1 Co atom, 26 Ce atoms, and 54 O atoms. During the optimization process, the bottom 6 atomic layers were kept fixed. The convergence criteria for electronic relaxation and ionic relaxation were established at 1 × 10^{-5} eV and 0.01 eV/Å, respectively. The cutoff energy of the plane wave basis was set to 480 eV, and a 3 × 3 × 1 Monkhorst−Pack k-point sampling was applied for the Brillouin zone. The binding energy ($E_{binding}$) can be calculated using the following equation:

$$E_{binding} = E_{surface+C_5H_8} - E_{surface} - E_{C_5H_8}$$

where $E_{surface+C_5H_8}$, $E_{surface}$, and $E_{C_5H_8}$ represent the energies of the surface with C_5H_8, the surface without C_5H_8, and a molecule of C_5H_8, respectively. The charge density difference plots were obtained using the following equation:

$$\Delta\rho = \rho_{surface+C_5H_8} - \rho_{surface} - \rho_{C_5H_8}$$

ASSOCIATED CONTENT

Supporting Information

The Supporting Information is available free of charge at https://pubs.acs.org/doi/10.1021/acsnano.4c03168.

Additional characterization data (SEM, XRD, XPS, TEM, STEM, EDS mapping, N_2 sorption isotherms, BJH pore size measurement, UPS) for the materials developed, particle size distribution of Co−CeO_2 NPs, transmittance spectra of CeO_2, Co−CeO_2 NPs, the average crystallite size of the materials developed calculated by the Scherrer equation, schematic illustrations of the gas sensor measurement system, data for control experiments (Fe−CeO_2@SnO_2 NFs, Ni−CeO_2@SnO_2 NFs, Pt@SnO_2 NFs), DFT-optimized binding configurations of CeO_2 and Co−CeO_2 toward the C_5H_8 molecule, detailed theoretical values from the DFT calculation, comparison of the performances of

https://doi.org/10.1021/acsnano.4c03168
ACS Nano 2024, 18, 19568−19580

sensing properties of the state-of-the-art C_5H_8 sensors compared with that of the Co−CeO_2@SnO_2 NF-based sensor reported in the literature, the price comparison table: price of metal per kilogram in USD as of April 16, 2024, a supplementary note detailing the preparation of Co−CeO_2 NPs (PDF)

AUTHOR INFORMATION

Corresponding Authors

Hee Jung Park − *Department of Materials Science and Engineering, Dankook University, Cheonan 31116, Republic of Korea;* orcid.org/0000-0001-8178-5345; Email: parkjang@dankook.ac.kr

Il-Doo Kim − *Department of Materials Science and Engineering, Korea Advanced Institute of Science and Technology (KAIST), Daejeon 34141, Republic of Korea;* orcid.org/0000-0002-9970-2218; Email: idkim@kaist.ac.kr

Authors

Jong Won Baek − *Department of Materials Science and Engineering, Korea Advanced Institute of Science and Technology (KAIST), Daejeon 34141, Republic of Korea*

Seunghee Han − *Department of Chemical and Biomolecular Engineering, Korea Advanced Institute of Science and Technology (KAIST), Daejeon 34141, Republic of Korea;* orcid.org/0000-0001-8696-6823

Sang Eun Lee − *Department of Materials Science and Engineering, Dankook University, Cheonan 31116, Republic of Korea*

Jaewan Ahn − *Department of Materials Science and Engineering, Korea Advanced Institute of Science and Technology (KAIST), Daejeon 34141, Republic of Korea;* orcid.org/0000-0002-0136-8427

Chungseong Park − *Department of Materials Science and Engineering, Korea Advanced Institute of Science and Technology (KAIST), Daejeon 34141, Republic of Korea*

Jong Seok Nam − *Department of Materials Science and Engineering, Korea Advanced Institute of Science and Technology (KAIST), Daejeon 34141, Republic of Korea*

Yoon Hwa Kim − *Department of Materials Science and Engineering, Korea Advanced Institute of Science and Technology (KAIST), Daejeon 34141, Republic of Korea*

Euichul Shin − *Department of Materials Science and Engineering, Korea Advanced Institute of Science and Technology (KAIST), Daejeon 34141, Republic of Korea*

Minhyun Kim − *Department of Materials Science and Engineering, Korea Advanced Institute of Science and Technology (KAIST), Daejeon 34141, Republic of Korea*

Ji-Soo Jang − *Electronic Materials Research Center, Korea Institute of Science and Technology, Seoul 02792, Republic of Korea;* orcid.org/0000-0001-6018-7231

Jihan Kim − *Department of Chemical and Biomolecular Engineering, Korea Advanced Institute of Science and Technology (KAIST), Daejeon 34141, Republic of Korea;* orcid.org/0000-0002-3844-8789

Complete contact information is available at: https://pubs.acs.org/10.1021/acsnano.4c03168

Author Contributions

J.W.B. designed the project, including the experiments with characterization, and wrote the manuscript. S.H. and J.K. conducted the computational analyses. J.A. and C.P. contributed to writing the manuscript and conducting formal analysis. S.E.L. and H.J.P. contributed to material synthesis. J.S.N., Y.H.K., and J.-S.J. contributed to the formal analysis. E.S. and M.K. contributed to formal analysis and gas sensing tests. I.-D.K. supervised this work and revised the manuscript.

Notes

The authors declare no competing financial interest.

ACKNOWLEDGMENTS

This work was supported by the Korea Technology and Information Promotion Agency for SMEs (Grant No. 00141845). This work was supported by the National Research Foundation of Korea (NRF) grant funded by the Korea government, Ministry of Science and ICT (Development of Nanofiber Yarn Based Compound Sensor as a Comprehensive Wearable Healthcare Solution) (Grant No. RS-2024-00357296). This work was also supported by the National Research Foundation of Korea (NRF) grant funded by the Korea government (MSIT) (No. RS-2023- 00236572).

REFERENCES

(1) Gas Sensor Market Size, Share and Growth Report, 2030 (Grand View Research), https://www.grandviewresearch.com/industry-analysis/gas-sensors-market. accessed 2023 August 28.

(2) Das, S.; Jayaraman, V. SnO_2: A comprehensive review on structures and gas sensors. *Prog. Mater. Sci.* **2014**, *66*, 112−255.

(3) Barsan, N.; Weimar, U. Conduction model of metal oxide gas sensors. *J. Electroceramics* **2001**, *7*, 143−167.

(4) Kim, S.-J.; Choi, S.-J.; Jang, J.-S.; Kim, N.-H.; Hakim, M.; Tuller, H. L.; Kim, I.-D. Mesoporous WO_3 nanofibers with protein-templated nanoscale catalysts for detection of trace biomarkers in exhaled breath. *ACS Nano* **2016**, *10*, 5891−5899.

(5) Kim, D.-H.; Cha, J.-H.; Shim, G.; Kim, Y. H.; Jang, J.-S.; Shin, H.; Ahn, J.; Choi, S.-Y.; Kim, I.-D. Flash-thermochemical engineering of phase and surface activity on metal oxides. *Chem* **2022**, *8*, 1014−1033.

(6) Zhu, L.-Y.; Ou, L.-X.; Mao, L.-W.; Wu, X.-Y.; Liu, Y.-P.; Lu, H.-L. Advances in Noble Metal-Decorated Metal Oxide Nanomaterials for Chemiresistive Gas Sensors: Overview. *Nano-Micro Lett.* **2023**, *15*, 89.

(7) Liotta, L. Catalytic oxidation of volatile organic compounds on supported noble metals. *Appl. Catal., B* **2010**, *100*, 403−412.

(8) Hansen, T. W.; DeLariva, A. T.; Challa, S. R.; Datye, A. K. Sintering of catalytic nanoparticles: particle migration or Ostwald ripening? *Acc. Chem. Res.* **2013**, *46*, 1720−1730.

(9) Zhang, F.; Zhu, Y.; Lin, Q.; Zhang, L.; Zhang, X.; Wang, H. Noble-metal single-atoms in thermocatalysis, electrocatalysis, and photocatalysis. *Energy Environ. Sci.* **2021**, *14*, 2954−3009.

(10) Korotcenkov, G.; Cho, B. Instability of metal oxide-based conductometric gas sensors and approaches to stability improvement (short survey). *Sens. Actuators, B* **2011**, *156*, 527−538.

(11) Azimi, G.; Dhiman, R.; Kwon, H.-M.; Paxson, A. T.; Varanasi, K. K. Hydrophobicity of rare-earth oxide ceramics. *Nat. Mater.* **2013**, *12*, 315−320.

(12) Branco, J. B.; Brito, P. E.; Ferreira, A. C. Methanation of CO_2 over nickel-lanthanide bimetallic oxides supported on silica. *Chem. Eng. J.* **2020**, *380*, 122465.

(13) Shi, X.; Cao, B.; Liu, J.; Zhang, J.; Du, Y. Rare-Earth-Based Metal−Organic Frameworks as Multifunctional Platforms for Catalytic Conversion. *Small* **2021**, *17* (22), 2005371.

(14) Montini, T.; Melchionna, M.; Monai, M.; Fornasiero, P. Fundamentals and catalytic applications of CeO_2-based materials. *Chem. Rev.* **2016**, *116*, 5987−6041.

(15) Su, Z.; Yang, W.; Wang, C.; Xiong, S.; Cao, X.; Peng, Y.; Si, W.; Weng, Y.; Xue, M.; Li, J. Roles of oxygen vacancies in the bulk and

surface of CeO_2 for toluene catalytic combustion. *Environ. Sci. Technol.* **2020**, *54*, 12684−12692.
(16) Jasinski, P.; Suzuki, T.; Anderson, H. U. Nanocrystalline undoped ceria oxygen sensor. *Sens. Actuators, B* **2003**, *95*, 73−77.
(17) Yuan, W.; Zhang, H.; Liu, Q.; Li, G.; Gao, X. Surface modification of $Li(Li_{0.17}Ni_{0.2}Co_{0.05}Mn_{0.58})O_2$ with CeO_2 as cathode material for Li-ion batteries. *Electrochim. Acta* **2014**, *135*, 199−207.
(18) Elias, J. S.; Risch, M.; Giordano, L.; Mansour, A. N.; Shao-Horn, Y. Structure, bonding, and catalytic activity of monodisperse, transition-metal-substituted CeO_2 nanoparticles. *J. Am. Chem. Soc.* **2014**, *136*, 17193−17200.
(19) Parastaev, A.; Muravev, V.; van Hoof, A. J.; Kimpel, T. F.; Kosinov, N.; Hensen, E. J. Boosting CO_2 hydrogenation via size-dependent metal−support interactions in cobalt/ceria-based catalysts. *Nat. Catal.* **2020**, *3*, 526−533.
(20) Kong, J.; Xiang, Z.; Li, G.; An, T. Introduce oxygen vacancies into CeO_2 catalyst for enhanced coke resistance during photo-thermocatalytic oxidation of typical VOCs. *Appl. Catal., B* **2020**, *269*, 118755.
(21) Koo, W.-T.; Choi, S.-J.; Kim, S.-J.; Jang, J.-S.; Tuller, H. L.; Kim, I.-D. Heterogeneous sensitization of metal−organic framework driven metal@ metal oxide complex catalysts on an oxide nanofiber scaffold toward superior gas sensors. *J. Am. Chem. Soc.* **2016**, *138*, 13431−13437.
(22) Baek, J. W.; Kim, Y. H.; Ahn, J.; Kim, D.-H.; Shin, H.; Ko, J.; Park, S.; Park, C.; Shin, E.; Jang, J.-S.; Kim, I.-D. Galvanic replacement reaction in perovskite oxide for superior chemiresistors. *J. Mater. Chem. A* **2022**, *10* (43), 23282−23293.
(23) Shin, H.; Kim, D.-H.; Jung, W.; Jang, J.-S.; Kim, Y. H.; Lee, Y.; Chang, K.; Lee, J.; Park, J.; Namkoong, K.; Kim, I.-D. Surface activity-tuned metal oxide chemiresistor: toward direct and quantitative halitosis diagnosis. *ACS Nano* **2021**, *15* (9), 14207−14217.
(24) Kang, J.-Y.; Jang, J.-S.; Koo, W.-T.; Seo, J.; Choi, Y.; Kim, M.-H.; Kim, D.-H.; Cho, H.-J.; Jung, W.; Kim, I.-D. Perovskite $La_{0.75}Sr_{0.25}Cr_{0.5}Mn_{0.5}O_{3-\delta}$ sensitized SnO_2 fiber-in-tube scaffold: Highly selective and sensitive formaldehyde sensing. *J. Mater. Chem. A* **2018**, *6*, 10543−10551.
(25) Kim, D.-H.; Kim, J. K.; Oh, D.; Park, S.; Kim, Y. B.; Ko, J.; Jung, W.; Kim, I.-D. Ex-Solution Hybrids Functionalized on Oxide Nanofibers for Highly Active and Durable Catalytic Materials. *ACS Nano* **2023**, *17*, 5842−5851.
(26) Baek, J. W.; Kim, I.-D. Advances in Perovskite Oxides for Chemiresistive Sensors. *Acc. Mater. Res.* **2023**, *4*, 1108−1120.
(27) Zhou, K.; Yang, Z.; Yang, S. Highly reducible CeO_2 nanotubes. *Chem. Mater.* **2007**, *19*, 1215−1217.
(28) Tok, A. I. Y.; Boey, F. Y. C.; Dong, Z.; Sun, X. Hydrothermal synthesis of CeO_2 nano-particles. *J. Mater. Process. Technol.* **2007**, *190*, 217−222.
(29) Mai, H.-X.; Sun, L.-D.; Zhang, Y.-W.; Si, R.; Feng, W.; Zhang, H.-P.; Liu, H.-C.; Yan, C.-H. Shape-selective synthesis and oxygen storage behavior of ceria nanopolyhedra, nanorods, and nanocubes. *J. Phys. Chem. B* **2005**, *109*, 24380−24385.
(30) Sahoo, T. R.; Armandi, M.; Arletti, R.; Piumetti, M.; Bensaid, S.; Manzoli, M.; Panda, S. R.; Bonelli, B. Pure and Fe-doped CeO_2 nanoparticles obtained by microwave assisted combustion synthesis: Physico-chemical properties ruling their catalytic activity towards CO oxidation and soot combustion. *Appl. Catal., B* **2017**, *211*, 31−45.
(31) Kang, W.; Ozgur, D. O.; Varma, A. Solution combustion synthesis of high surface area CeO_2 nanopowders for catalytic applications: reaction mechanism and properties. *ACS Appl. Nano Mater.* **2018**, *1*, 675−685.
(32) Yang, W.; Li, C.; Wang, H.; Li, X.; Zhang, W.; Li, H. Cobalt doped ceria for abundant storage of surface active oxygen and efficient elemental mercury oxidation in coal combustion flue gas. *Appl. Catal., B* **2018**, *239*, 233−244.
(33) Basina, G.; Polychronopoulou, K.; Zedan, A. F.; Dimos, K.; Katsiotis, M. S.; Fotopoulos, A. P.; Ismail, I.; Tzitzios, V. Ultrasmall metal-doped CeO_2 nanoparticles for low-temperature CO oxidation. *ACS Appl. Nano Mater.* **2020**, *3*, 10805−10813.
(34) Carvalho, J.; Rocha, L.; Renzetti, R.; Procopio, A.; Mastelaro, V. R.; Simões, A.; Ponce, M.; Macchi, C.; Somoza, A.; Aldao, C.; Longo, E.; et al. High-performance CeO_2: Co nanostructures for the elimination of accidental poisoning caused by CO intoxication. *Open Ceram.* **2022**, *12*, 100298.
(35) Tiwari, A.; Bhosle, V. M.; Ramachandran, S.; Sudhakar, N.; Narayan, J.; Budak, S.; Gupta, A. Ferromagnetism in Co doped CeO_2: Observation of a giant magnetic moment with a high Curie temperature. *Appl. Phys. Lett.* **2006**, *88*, 142511.
(36) Mohanapriya, S.; Priyadharshini, P.; Shobika, P.; Ponnar, M.; Pushpanathan, K. Effect of Co dopant on structural, optical, and magnetic properties of CeO_2 quantum dots. *J. Aust. Ceram. Soc.* **2023**, *59*, 459−480.
(37) Al-Hashem, M.; Akbar, S.; Morris, P. Role of oxygen vacancies in nanostructured metal-oxide gas sensors: a review. *Sens. Actuators, B* **2019**, *301*, 126845.
(38) Kutin, Y.; Cox, N.; Lubitz, W.; Schnegg, A.; Rüdiger, O. *In situ* EPR characterization of a cobalt oxide water oxidation catalyst at neutral pH. *Catalysts* **2019**, *9*, 926.
(39) Khan, M. E.; Khan, M. M.; Cho, M. H. Ce^{3+}-ionSurface Oxygen Vacancy, and Visible Light-induced Photocatalytic Dye Degradation and Photocapacitive Performance of CeO_2-Graphene Nanostructures. *Sci. Rep.* **2017**, *7* (1), 5928.
(40) Li, J.; Wang, Y.; Lu, X.; Guo, K.; Xu, C. Increased Oxygen Vacancies in CeO_2 for Improved Electrocatalytic Nitrogen Reduction Performance. *Inorg. Chem.* **2022**, *61*, 17242−17247.
(41) Zimou, J.; Nouneh, K.; Hsissou, R.; El-Habib, A.; El Gana, L.; Talbi, A.; Beraich, M.; Lotfi, N.; Addou, M. Structural, morphological, optical, and electrochemical properties of Co-doped CeO_2 thin films. *Mater. Sci. Semicond.* **2021**, *135*, 106049.
(42) Venkataswamy, P.; Jampaiah, D.; Kandjani, A. E.; Sabri, Y. M.; Reddy, B. M.; Vithal, M. Transition (Mn, Fe) and rare earth (La, Pr) metal doped ceria solid solutions for high performance photocatalysis: Effect of metal doping on catalytic activity. *Res. Chem. Intermed.* **2018**, *44*, 2523−2543.
(43) Slavinskaya, E.; Zadesenets, A.; Stonkus, O.; Stadnichenko, A.; Shchukarev, A.; Shubin, Y. V.; Korenev, S.; Boronin, A. Thermal activation of Pd/CeO_2-SnO_2 catalysts for low-temperature CO oxidation. *Appl. Catal., B* **2020**, *277*, 119275.
(44) Ahn, H.-J.; Choi, H.-C.; Park, K.-W.; Kim, S.-B.; Sung, Y.-E. Investigation of the structural and electrochemical properties of size-controlled SnO_2 nanoparticles. *J. Phys. Chem. B* **2004**, *108*, 9815−9820.
(45) Wang, D.; Wan, K.; Zhang, M.; Li, H.; Wang, P.; Wang, X.; Yang, J. Constructing hierarchical SnO_2 nanofiber/nanosheets for efficient formaldehyde detection. *Sens. Actuators, B* **2019**, *283*, 714−723.
(46) Korotcenkov, G. The role of morphology and crystallographic structure of metal oxides in response of conductometric-type gas sensors. *Mater. Sci. Eng. R Rep.* **2008**, *61*, 1−39.
(47) Hori, A.; Suijo, K.; Kondo, T.; Hotta, N. Breath isoprene excretion during rest and low-intensity cycling exercise is associated with skeletal muscle mass in healthy human subjects. *J. Breath Res.* **2021**, *15*, 016009.
(48) Karl, T.; Prazeller, P.; Mayr, D.; Jordan, A.; Rieder, J.; Fall, R.; Lindinger, W. Human breath isoprene and its relation to blood cholesterol levels: new measurements and modeling. *J. Appl. Physiol.* **2001**, *91*, 762−770.
(49) Gurlo, A.; Riedel, R. *In situ* and operando spectroscopy for assessing mechanisms of gas sensing. *Angew. Chem., Int. Ed.* **2007**, *46*, 3826−3848.
(50) Han, B.; Wang, J.; Yang, W.; Chen, X.; Wang, H.; Chen, J.; Zhang, C.; Sun, J.; Wei, X. Hydrothermal synthesis of flower-like In_2O_3 as a chemiresistive isoprene sensor for breath analysis. *Sens. Actuators, B* **2020**, *309*, 127788.
(51) Wu, X.; Wang, H.; Wang, J.; Chen, J.; Shi, L.; Han, B.; Tian, X. Hydrothermal synthesis of flower-like Cr_2O_3-doped In_2O_3 nanorods clusters for ultra-low isoprene detection. *Colloids Surf. A: physicochem. Eng. Asp.* **2021**, *620*, 126606.

https://doi.org/10.1021/acsnano.4c03168
ACS Nano 2024, 18, 19568−19580

(52) Han, B.; Wang, H.; Yang, W.; Wang, J.; Wei, X. Hierarchical Pt-decorated In_2O_3 microspheres with highly enhanced isoprene sensing properties. *Ceram. Int.* **2021**, *47*, 9477−9485.
(53) Park, Y.; Yoo, R.; Ryull Park, S.; Lee, J. H.; Jung, H.; Lee, H.-S.; Lee, W. Highly sensitive and selective isoprene sensing performance of ZnO quantum dots for a breath analyzer. *Sens. Actuators, B* **2019**, *290*, 258−266.
(54) van den Broek, J.; Guntner, A. T.; Pratsinis, S. E. Highly selective and rapid breath isoprene sensing enabled by activated alumina filter. *ACS Sens* **2018**, *3*, 677−683.
(55) Güntner, A. T.; Pineau, N. J.; Chie, D.; Krumeich, F.; Pratsinis, S. E. Selective sensing of isoprene by Ti-doped ZnO for breath diagnostics. *J. Mater. Chem. B* **2016**, *4*, 5358−5366.
(56) Teleki, A.; Pratsinis, S. E.; Kalyanasundaram, K.; Gouma, P. Sensing of organic vapors by flame-made TiO_2 nanoparticles. *Sens. Actuators, B* **2006**, *119*, 683−690.
(57) Xing, X.; Du, L.; Wang, C.; Feng, D.; Liu, G.; Yang, D. ZIF-8 micro-polyhedron MOF-transformed $ZnO/ZnFe_2O_4$ nanosheets for highly selective detection of ppb-level isoprene. *Sens. Actuators, B* **2022**, *372*, 132669.
(58) Guo, X. H.; Mao, C. C.; Zhang, J.; Huang, J.; Wang, W. N.; Deng, Y. H.; Wang, Y. Y.; Cao, Y.; Huang, W. X.; Yu, S. H. Cobalt-Doping-Induced Synthesis of Ceria Nanodisks and Their Significantly Enhanced Catalytic Activity. *Small* **2012**, *8*, 1515.
(59) Gurlo, A. Interplay between O_2 and SnO_2: oxygen ionosorption and spectroscopic evidence for adsorbed oxygen. *ChemPhyschem* **2006**, *7*, 2041−2052.
(60) Sopiha, K. V.; Malyi, O. I.; Persson, C.; Wu, P. Chemistry of oxygen ionosorption on SnO_2 surfaces. *ACS Appl. Mater. Interfaces* **2021**, *13*, 33664−33676.
(61) Kresse, G.; Furthmüller, J. Efficiency of ab-initio total energy calculations for metals and semiconductors using a plane-wave basis set. *Comput. Mater. Sci.* **1996**, *6*, 15−50.
(62) Kresse, G.; Hafner, J. Ab initio molecular dynamics for liquid metals. *Phys. Rev. B* **1993**, *47*, 558.
(63) Kresse, G.; Joubert, D. From ultrasoft pseudopotentials to the projector augmented-wave method. *Phys. Rev. B* **1999**, *59*, 1758.
(64) Grimme, S.; Antony, J.; Ehrlich, S.; Krieg, H. A consistent and accurate ab initio parametrization of density functional dispersion correction (DFT-D) for the 94 elements H-Pu. *J. Chem. Phys.* **2010**, *132*, 154104.
(65) Jain, A.; Ong, S. P.; Hautier, G.; Chen, W.; Richards, W. D.; Dacek, S.; Cholia, S.; Gunter, D.; Skinner, D.; Ceder, G.; Persson, K. A. Commentary: The Materials Project: A materials genome approach to accelerating materials innovation. *APL Mater.* **2013**, *1* (1), 011002.
(66) Conesa, J. Computer modeling of surfaces and defects on cerium dioxide. *Surf. Sci.* **1995**, *339*, 337−352.

https://doi.org/10.1021/acsnano.4c03168
ACS Nano 2024, 18, 19568−19580